

Regimes of thermo-compositional convection and related dynamos in rotating spherical shells

James F. Mather¹ and Radostin D. Simatev²

School of Mathematics and Statistics, University of Glasgow – Glasgow G12 8QQ, UK

(Submitted to *GAFD* 2019-07-16; Accepted to *GAFD* 2020-04-24)

Convection and magnetic field generation in the Earth and planetary interiors are driven by both thermal and compositional gradients. In this work numerical simulations of finite-amplitude double-diffusive convection and dynamo action in rapidly rotating spherical shells full of incompressible two-component electrically-conducting fluid are reported. Four distinct regimes of rotating double-diffusive convection identified in a recent linear analysis (Silva et al., 2019, *Geophys. Astrophys. Fluid Dyn.*, doi:10.1080/03091929.2019.1640875) are found to persist significantly beyond the onset of instability while their regime transitions remain abrupt. In the semi-convecting and the fingering regimes characteristic flow velocities are small compared to those in the thermally- and compositionally-dominated overturning regimes, while zonal flows remain weak in all regimes apart from the thermally-dominated one. Compositionally-dominated overturning convection exhibits significantly narrower azimuthal structures compared to all other regimes while differential rotation becomes the dominant flow component in the thermally-dominated case as driving is increased. Dynamo action occurs in all regimes apart from the regime of fingering convection. While dynamos persist in the semi-convective regime they are very much impaired by small flow intensities and very weak differential rotation in this regime which makes poloidal to toroidal field conversion problematic. The dynamos in the thermally-dominated regime include oscillating dipolar, quadrupolar and multipolar cases similar to the ones known from earlier parameter studies. Dynamos in the compositionally-dominated regime exhibit subdued temporal variation and remain predominantly dipolar due to weak zonal flow in this regime. These results significantly enhance our understanding of the primary drivers of planetary core flows and magnetic fields.

Keywords: Double-diffusive convection; Buoyancy-driven instabilities; Dynamo action; Planetary cores;

1. Introduction

Convective flows and magnetic field generation in Earth’s fluid outer core are driven by a combination of thermal and chemical composition gradients (Kono 2002, Jones 2015, Wicht and Sanchez 2019). Rotating double-diffusive convection is also likely to occur in and affect the magnetic properties of other planets including Mercury (Breuer *et al.* 2007), Venus (Jacobson *et al.* 2017), Jupiter (Moll *et al.* 2017) and Saturn (Lecante and Chabrier 2012) as well as many stellar objects (Garaud 2018).

Numerical models of global planetary and core convection and dynamos have been predominantly single-diffusive (Jones 2011). Either purely thermal convection was assumed or the so called “co-density” formulation (Braginsky and Roberts 1995) was used to effectively replace temperature and concentration by a single field variable. A notable exception is the celebrated early geodynamo model of Glatzmaier and Roberts (1996) where separate thermal and compositional buoyancies were used but identical values for the thermal and chemical diffusivity were set thus excluding double-diffusive effects. However, single-diffusive convection models fail to account for significant differences in the diffusivities of heat and chemical constituents as well as for essential differences in boundary conditions and sink/source distributions of

¹ orcid.org/0000-0001-9518-0515

² Radostin.Simatev@glasgow.ac.uk, orcid.org/0000-0002-2207-5789

the temperature and of the constituent concentration field (Jones 2015). In the last decade several authors have recognized these limitations and have sought to investigate explicitly double-diffusive thermo-compositional effects on convection flows and dynamo processes in rapidly-rotating spheres and shells. Using two separate equations for the temperature and for the concentration of light constituents, respectively, Breuer *et al.* (2010) observed an abrupt change in convective regime when the relative contribution of compositional driving exceeds 20%. In a similar model, Trümper *et al.* (2012) considered the effect of distinct boundary conditions for temperature and concentration and obtained preliminary results on the onset of convection using an initial value code. Simulating a double-diffusive model of Mercury’s dynamo, Manglik *et al.* (2010) observed that when thermal and compositional buoyancy are of equal intensity, a stratified outer layer is formed and is then penetrated by fingering convection that in turn enhances the poloidal magnetic field, a significant difference compared to co-density cases. Reporting some 20 numerical dynamo runs, Takahashi (2014) found that, due to helicity increase, magnetic fields have predominantly non-dipolar morphology when compositional buoyancy is less than 40% of the total driving and predominantly dipolar one otherwise. In short, significant thermo-compositional effects were found in all of the latter works. However, these studies were largely limited to numerical runs isolated in the configuration space and considered the case of when the thermal buoyancy and the compositional buoyancy are both destabilising.

Systematic parameter studies of the linear onset of double-diffusive convection in rotating spherical shells were undertaken by Net *et al.* (2012) and recently by Silva *et al.* (2019). Following Simitev (2011), the study of Silva *et al.* (2019) confirmed that due to distinct “double-diffusive” eigenmodes, critical curves for the onset of thermo-compositional instability are generally multi-valued and form what may be described as “pockets” of instability protruding regions of quiescence. Situations thus arise whereby increasing the thermal or the compositional driving leads to onset of instability at the entry of a pocket and a subsequent return to quiescence as driving is further increased to exit the pocket. The pockets of instability are closely related to transitions between four different regimes of rapidly-rotating double-diffusive convection that can be identified as semi-convection, fingering convection, thermally-dominated overturning convection and chemically dominated overturning convection. The onset of these regimes were mapped by Silva *et al.* (2019) who probed a significant portion of the configuration space by varying the values of all governing parameters.

The main goals of the present work are (a) to establish the possibility of dynamo action arising due to double-diffusive flows on stably stratified background, in other words in the regimes of semi-diffusive and fingering flows, and (b) to assess how dynamos generated by thermally- and chemically-dominated overturning convection differ from each other. Before these goals can be addressed, it is necessary to (c) trace out the flow regime boundaries in the non-linear domain. While rotating double-diffusive convection at finite amplitude was recently studied by Monville *et al.* (2019), essential differences with our model remain since full spherical geometry, no-slip velocity conditions and mainly the semi-convective regime were considered by these authors. Thus, using as a starting point the linear results of Silva *et al.* (2019), we perform parameter continuation increasing the thermal and compositional Rayleigh numbers (defined further below) beyond onset. For the sake of comparison, we keep most other governing parameters fixed to values where purely thermal convection and dynamo solutions are well studied in the literature. Even with these restrictions, results from over 80 new finite-amplitude thermo-compositional convection simulations and over 30 dynamo simulations are summarized below. We take the opportunity, to assess to what extent instability pockets survive nonlinear interactions; the structure and intensity of zonal and other flow components; observe how magnetic field morphology and symmetry change across the regime boundaries and describe the time-dependent behaviour of solutions and investigate whether dynamos close to each other in the parameter space can exhibit widely different morphol-

ogy and behaviour. These questions are relevant to understanding the geomagnetic field at present and in geological time as well as to understanding the zoo of other planetary and stellar magnetic fields.

Beyond spherical models, there has been a significant interest in astrophysical applications of double-diffusive convection in recent years (Garaud 2018). Asymptotic scaling laws for turbulent heat and compositional transport have been proposed and spontaneous layering has been investigated at small values of the Prandtl number for both the fingering regime (Traxler *et al.* 2011, Brown *et al.* 2013) and the semi-convective regime (Mirouh *et al.* 2012, Wood *et al.* 2013, Moll *et al.* 2016). These results complement our analysis but direct application to the case reported here remains difficult. This is because a local “unbounded gradient layer” model (Radko 2013) in a triply periodic box is used in the latter works to minimize the effect of boundaries and to exclude overturning flows from the analysis. In contrast, we aim to capture all regimes of global-scale rotating thermo-compositional convection in spherical geometry and thus employ a “vertically bounded layer” model of the type proposed by Veronis (1968).

2. Mathematical model

We follow standard mathematical formulations of the problem of rotating spherical dynamos e.g. (Simatev and Busse 2005) modified by introducing a separate equation for the chemical concentration of the form used in (Silva *et al.* 2019). In detail, we consider a two-component electrically conducting fluid confined to a spherical shell rotating with a fixed angular velocity $\Omega\hat{\mathbf{k}}$, where $\hat{\mathbf{k}}$ is the unit vector in the direction of the axis of rotation. The inner and outer spherical surfaces, $r = r_i$ and $r = r_o$, respectively, are kept at constant values of the temperature and of the concentration of the light element. The gravity field is assumed in the form $\mathbf{g} = -\gamma d\mathbf{r}$ where \mathbf{r} is the position vector with respect to the center of the sphere and r is its length measured in units of the thickness d of the spherical shell. Assuming volumetric sources/sinks of thermal and compositional buoyancy with constant densities β_T and β_C , respectively, a static state exists with temperature and concentration profiles given by

$$T_S = T_0 - \frac{\beta_T}{2}r^2, \quad C_S = C_0 - \frac{\beta_C}{2}r^2, \quad (1)$$

respectively. Here T_0 and C_0 are constant reference values of temperature and concentration. We employ the Boussinesq approximation in that all material properties of the fluid are assumed constant except the density which is taken to depend on temperature and concentration so the following truncated Taylor expansion near its reference value ρ_0 is used when it enters the buoyancy term

$$\rho = \rho_0(1 - \alpha_T\Theta - \alpha_C\Gamma),$$

where α_T and α_C are the specific thermal and compositional coefficients of expansion/contraction, and Θ and Γ are the deviations from the temperature and the concentration basic static states T_S and C_S given by equations (1). The length d , the time d^2/ν , the temperature $\nu^2/\gamma\alpha_T d^4$ and composition $\nu^2/\gamma\alpha_C d^4$ are used as scales for the dimensionless description of the problem where ν denotes the kinematic viscosity. The dimensionless governing equations of momentum, temperature, concentration, magnetic induction and the conditions of incompressibility of the fluid and solenoidality of the magnetic field are then given by

$$(\partial_t + \mathbf{u} \cdot \nabla)\mathbf{u} + \tau\mathbf{k} \times \mathbf{u} = -\nabla\pi + (\Theta + \Gamma)\mathbf{r} + \nabla^2\mathbf{u} + (\nabla \times \mathbf{B}) \times \mathbf{B}, \quad (2a)$$

$$\nabla \cdot \mathbf{u} = 0, \quad (2b)$$

$$\text{Pr}(\partial_t + \mathbf{u} \cdot \nabla)\Theta = R_T\mathbf{r} \cdot \mathbf{u} + \nabla^2\Theta, \quad (2c)$$

$$\text{Sc}(\partial_t + \mathbf{u} \cdot \nabla)\Gamma = R_C\mathbf{r} \cdot \mathbf{u} + \nabla^2\Gamma, \quad (2d)$$

$$\partial_t \mathbf{B} = \nabla \times (\mathbf{u} \times \mathbf{B}) + \text{Pm}^{-1} \nabla^2 \mathbf{B}, \quad (2e)$$

$$\nabla \cdot \mathbf{B} = 0, \quad (2f)$$

where \mathbf{u} and \mathbf{B} are the velocity and the magnetic field vectors, respectively, and π denotes an effective pressure field representing all terms that can be expressed as a gradient. Eight dimensionless numbers appear in the equations, namely, the shell radius ratio, the thermal Rayleigh number R_T , the compositional Rayleigh number R_C , the Coriolis parameter τ , the Prandtl number Pr , the Schmidt number Sc and the magnetic Prandtl number Pm defined as

$$\eta = \frac{r_i}{r_o}, \quad R_T = \frac{\alpha_T \gamma \beta_T d^6}{\nu \kappa}, \quad R_C = \frac{\alpha_C \gamma \beta_C d^6}{\nu D}, \quad \tau = \frac{2\Omega d^2}{\nu}, \quad \text{Pr} = \frac{\nu}{\kappa}, \quad \text{Sc} = \frac{\nu}{D}, \quad \text{Pm} = \frac{\nu}{\lambda}, \quad (3)$$

respectively. Here, κ denotes the thermal diffusivity, D denotes the mass diffusivity and λ denotes the magnetic diffusivity.

Since the velocity and the magnetic field are both solenoidal the general representation in terms of poloidal and toroidal components can be used,

$$\mathbf{u} = \nabla \times (\nabla v \times \mathbf{r}) + \nabla w \times \mathbf{r}, \quad \mathbf{B} = \nabla \times (\nabla h \times \mathbf{r}) + \nabla g \times \mathbf{r}.$$

By multiplying the (curl)² and the curl of the momentum equation (2a) by \mathbf{r} we obtain two equations for the poloidal and toroidal scalar fields of the velocity, v and w ,

$$((\nabla^2 - \partial_t)L_2 + \tau \partial_\varphi) \nabla^2 v + \tau Q w - L_2(\Theta + \Gamma) = -\mathbf{r} \cdot \nabla \times \nabla \times (\mathbf{u} \cdot \nabla \mathbf{u} - \mathbf{B} \cdot \nabla \mathbf{B}), \quad (4a)$$

$$((\nabla^2 - \partial_t)L_2 + \tau \partial_\varphi) w - \tau Q v = \mathbf{r} \cdot \nabla \times (\mathbf{u} \cdot \nabla \mathbf{u} - \mathbf{B} \cdot \nabla \mathbf{B}). \quad (4b)$$

The temperature and the concentration equations may be written as follows

$$\nabla^2 \Theta + R_T L_2 v = \text{Pr}(\partial_t + \mathbf{u} \cdot \nabla) \Theta, \quad (4c)$$

$$\nabla^2 \Gamma + R_C L_2 v = \text{Sc}(\partial_t + \mathbf{u} \cdot \nabla) \Gamma. \quad (4d)$$

The equations for poloidal and toroidal scalar of the magnetic field, h and g , are obtained by multiplication of (2e) and of its curl by \mathbf{r}

$$\nabla^2 L_2 h = \text{Pm}(\partial_t L_2 h - \mathbf{r} \cdot \nabla \times (\mathbf{u} \times \mathbf{B})), \quad (4e)$$

$$\nabla^2 L_2 g = \text{Pm}(\partial_t L_2 g - \mathbf{r} \cdot \nabla \times \nabla \times (\mathbf{u} \times \mathbf{B})). \quad (4f)$$

In the above, ∂_t and ∂_φ denote the partial derivatives with respect to time t and with respect to the angle φ of a spherical system of coordinates r, θ, φ and the operators L_2 and Q are defined by

$$L_2 \equiv -r^2 \nabla^2 + \partial_r(r^2 \partial_r),$$

$$Q \equiv r \cos \theta \nabla^2 - (L_2 + r \partial_r)(\cos \theta \partial_r - r^{-1} \sin \theta \partial_\theta).$$

Stress-free boundaries with fixed temperature and concentration values are assumed,

$$v = \partial_{rr}^2 v = \partial_r(w/r) = \Theta = \Gamma = 0 \quad \text{at} \quad r = r_i, \quad r = r_o, \quad (5a)$$

where $r_i = \eta/(1 - \eta)$ and $r_o = (1 - \eta)^{-1}$. For the magnetic field, electrically insulating boundaries are assumed in such a way that the poloidal function h is matched to the function $h^{(e)}$ which describes the potential fields outside the fluid shell

$$g = h - h^{(e)} = \partial_r(h - h^{(e)}) = 0 \quad \text{at} \quad r = r_i, \quad r = r_o. \quad (5b)$$

The use of Dirichlet conditions for temperature and concentration and of stress-free boundaries is a modeling simplification made for several reasons. First as discussed, we essentially rely on the linear results of [Silva et al. \(2019\)](#) which were obtained with this choice of boundary conditions in order to isolate the effects induced by differences in thermal and concentration

diffusivities from the effects induced by differences in boundary conditions and in source/sink distributions. Second, there is no universal agreement on the most appropriate choice of boundary conditions even for the best-known planetary core, that of the Earth. In Earth’s core, rigid flow boundary conditions at both boundaries seem appropriate. However, in common with all simulations reported in the literature, the Coriolis number τ we use is many orders of magnitude too small and the viscous Ekman boundary layers, whose thickness scales like $\tau^{-1/2}$ becomes much more dominant in the simulations than it is in reality. We follow e.g. (Kuang and Bloxham 1997, Busse and Simitev 2011, Aubert 2012) and use stress-free conditions to alleviate this. A detailed comparison of no-slip and stress-free models of the dynamics of rapidly rotating fluid in a spherical shell has been reported by (Livermore *et al.* 2016), also see the review of Roberts and King (2013). The inner core is a source for heat and light elements and it is appropriate to model this by fixed flux conditions for Θ and Γ . Indeed, the composition flux has to vanish at the core-mantle boundary as chemical elements cannot penetrate it. Heat flux at the core-mantle boundary can be related to lower mantle temperature as the mantle evolves on timescales much longer than these of the outer core. However, the thermal and compositional boundary conditions at the interface to a growing inner iron core are likely even more involved, in that, the temperature flux and the compositional flux are related to each other via a coupled set of differential equations (Braginsky and Roberts 1995, Glatzmaier and Roberts 1996). Furthermore, it is uncertain how a seismologically distinct mushy or slurry F-layer at base of Earth’s outer core may be (Wong *et al.* 2018) affect boundary conditions. The outer boundary of the convective regions of gas planets and stars requires yet different boundary conditions, see discussion in (Wicht and Tilgner 2010). Various choices of thermal and compositional boundary conditions were investigated by (Hori *et al.* 2012).

3. Numerical methods and diagnostics

3.1. Methods and code

For the direct numerical integration of the problem defined by the scalar equations (4) and the boundary conditions (5) we use a pseudo-spectral method described by Tilgner (1999). A code used by us for a number of years (Busse *et al.* 2003, Busse and Simitev 2011, Simitev *et al.* 2015) and benchmarked for accuracy most recently in (Marti *et al.* 2014, Matsui *et al.* 2016) was adapted to include the additional equation for the chemical concentration of light elements (4d). The code has been made open source (Silva and Simitev 2018). We briefly mention here that the spatial discretisation is based on an expansion of all dependent variables in spherical harmonics for the angular dependences and in Chebychev polynomials for the radial dependence, e.g. the expansion of the poloidal scalar function takes the form

$$v(r, \theta, \varphi) = \sum_{l,m,n}^{N_l, N_m, N_n} V_{l,n}^m(t) T_n(x(r)) P_l^m(\theta) \exp(im\varphi), \quad (6)$$

with $x(r) = 2(r - r_i) - 1$, and analogous expressions for the other dynamical variables, w , h , g , Θ and Γ are used. Here P_l^m denotes the associated Legendre polynomials of degree l and order m and T_n denotes the Chebychev polynomials of degree n . The computation of nonlinear terms in spectral space is, however, expensive so all nonlinear products and the Coriolis term are computed in the physical space and then projected onto the spectral space at every time step. A hybrid combination of the Crank–Nicolson scheme for the diffusion terms and the second order Adams–Bashforth scheme for the nonlinear terms is used for time-stepping.

3.2. Resolution and convergence

Spherical harmonics truncation of $N_l = N_m = 144$ and up to $N_r = 51$ collocation points in radial direction have been used and a time step of the order 10^{-6} was typically required for the computations reported below. Calculations are considered resolved when the spectral power of kinetic and magnetic energy drops by more than a factor of 100 from the spectral maximum to the cut-off wavelength, a criterion commonly used e.g. (Christensen *et al.* 1999). Typical spectra are shown further below in figure 8. We have evolved dynamo simulations for at least one ohmic diffusion time and hydrodynamic simulations for at least one viscous diffusion time in most cases for much longer as seen in the time series included in figure 8. All time averages are calculated after removing transient periods of the simulations.

3.3. Diagnostics

To analyse the properties of the solution we typically monitor kinetic and magnetic energy components. In particular, we decompose the kinetic energy density into poloidal and toroidal parts (respectively denoted by subscripts as in X_p and X_t in equations (7) below and where X denotes an appropriate quantity) and further into mean (axisymmetric) and fluctuating (nonaxisymmetric) components (respectively denoted by bars and tildes as in \bar{X} and \tilde{X} below) and into equatorially-symmetric and equatorially-antisymmetric components (respectively denoted by superscripts as in X^s and X^a below),

$$\begin{aligned} \bar{E}_p &= \bar{E}_p^s + \bar{E}_p^a = \frac{1}{2} \left\langle (\nabla \times (\nabla(\bar{v}^s + \bar{v}^a) \times \mathbf{r}))^2 \right\rangle, \\ \bar{E}_t &= \bar{E}_t^s + \bar{E}_t^a = \frac{1}{2} \left\langle (\nabla r(\bar{w}^s + \bar{w}^a) \times \mathbf{r})^2 \right\rangle, \\ \tilde{E}_p &= \tilde{E}_p^s + \tilde{E}_p^a = \frac{1}{2} \left\langle (\nabla \times (\nabla(\tilde{v}^s + \tilde{v}^a) \times \mathbf{r}))^2 \right\rangle, \\ \tilde{E}_t &= \tilde{E}_t^s + \tilde{E}_t^a = \frac{1}{2} \left\langle (\nabla r(\tilde{w}^s + \tilde{w}^a) \times \mathbf{r})^2 \right\rangle, \end{aligned} \tag{7}$$

where angular brackets $\langle \rangle$ denote averages over the volume of the spherical shell. Since in our code the spectral representation of all fields X is given by the set of coefficients $\{X_l^m\}$ of their expansions in spherical harmonics Y_l^m , it is easy to extract the relevant components, i.e. coefficients with $m = 0$ and with $m \neq 0$ represent axisymmetric and nonaxisymmetric components, respectively, while coefficients with even $(l + m)$ and with odd $(l + m)$ represent equatorially-symmetric and equatorially-antisymmetric components, respectively. The magnetic energy density is similarly decomposed into components. The time averaged Reynolds number is defined as

$$\text{Re} = \sqrt{2E},$$

where $E = \bar{E}_p + \bar{E}_t + \tilde{E}_p + \tilde{E}_t$, is the total kinetic energy density.

4. The onset of rotating double-diffusive convection

A systematic investigation of the onset of double-diffusive convection in rotating spherical shells is reported in (Silva *et al.* 2019). In this section, we summarize very briefly selected linear results of this study since these will be used as a base for tracing out the boundaries of thermo-compositional regimes in the non-linear domain.

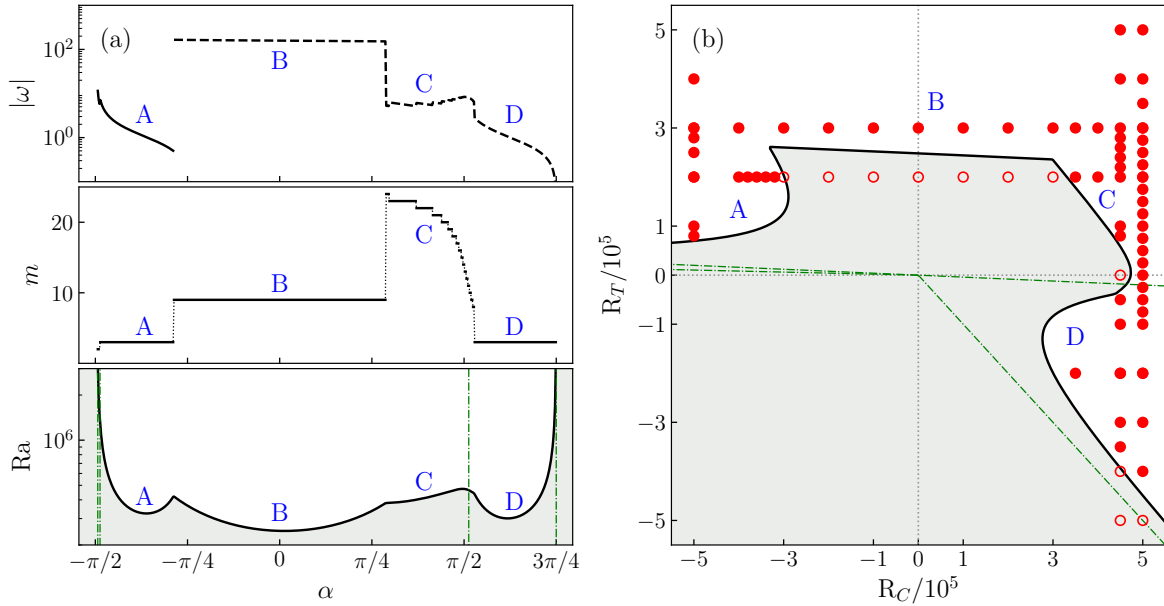


Figure 1. Critical curves for the onset of convection and selected finite-amplitude non-magnetic runs in the case $\text{Pr} = 1$, $\text{Sc} = 25$, $\tau = 10^4$, $\eta = 0.35$. (a) Critical curves as a function of the mixing angle α as follows. Top panel: the magnitude of the critical drift rate $|\omega|$ at onset; prograde direction (negative drift rate) indicated by broken line, retrograde direction (positive drift rate) indicated by solid line. Middle panel: values of the critical azimuthal wave-number m at onset. Bottom panel: values of the critical effective Rayleigh number Ra . (b) The critical curve in the $R_C - R_T$ plane is shown as a black solid line. The positions in the parameter space of selected supercritical and subcritical finite-amplitude runs are indicated with full and empty red circles, respectively. In both panels (a) and (b): The subcritical region of no convection is shaded in light-grey. Blue letters A, B, C, and D denote the approximate location of the regimes of rotating semi-convection, rotating thermally-dominated overturning convection, rotating compositionally-dominated overturning convection and rotating fingering convection, respectively, as discussed in the text. In clockwise direction in (b) and from left to right in the bottom panel of (a) green dash-dotted lines mark the stability bounds $R_T = -(\text{Pr} + 1/\text{Le})R_C/(\text{Le}(\text{Pr} + 1))$, $R_T = -R_C/\text{Le}$, $R_T = -R_C/\text{Le}$ and $R_T = -R_C$, respectively, see equations (9). (Colour online)

4.1. Onset at selected parameters

Figure 1 shows the critical Rayleigh numbers R_T and R_C , the preferred azimuthal wave number m and drift rate ω for the onset of instability at other parameter values fixed to

$$\text{Pr} = 1, \quad \text{Sc} = 25, \quad \tau = 10^4, \quad \eta = 0.35, \quad \text{Pm} = 0. \quad (8)$$

The Lewis number defined as $\text{Le} = \text{Sc}/\text{Pr}$ is sometimes used in the literature instead of the Schmidt number Sc , e.g. (Simatev 2011, Monville *et al.* 2019). In our study the value of the Lewis number is kept fixed to $\text{Le} = 25$ throughout. To facilitate direct comparison with (Silva *et al.* 2019), in the left panel (a) of the figure a re-parametrisation is used where a ‘total effective’ Rayleigh number and a mixing angle α are introduced as follows

$$\text{Ra} = \sqrt{R_T^2 + R_C^2}, \quad \alpha = \text{atan2}(R_C, R_T).$$

Here the function $\text{atan2}(y, x)$ is defined for $x \in \mathbb{R}$, $y \in \mathbb{R}$ as the principal argument $\text{Arg}(z)$ of the complex number $z = x + iy$, a notation used in many programming languages. The more conventional representation of the critical curves in the $R_C - R_T$ plane is shown in the right panel figure 1(b). Four convective regimes are immediately discernible – semi-convection, thermally-dominated overturning convection, compositionally-dominated overturning convection and fingering convection. For convenience, these regimes are labeled by A, B, C and D, respectively in figures and discussion throughout. Regime A occurs for values of the mixing angle α between $-\pi/2$ and $-5\pi/16$. This regime was identified in (Silva *et al.* 2019) as semi-convection as it occurs at negative values of R_C and positive values of R_T which in our model corresponds to cooler and lighter fluid over warmer and heavier fluid. The linear analysis indi-

cates that flows in this regime consist of large spatial structures with azimuthal wave number $m = 3$ drifting in retrograde direction ($\omega > 0$). An abrupt transition to a different regime B occurs at values of the mixing angle of about $\alpha \approx -5\pi/16$ and persists up to $\alpha \approx 5\pi/16$. Within this range the critical curve is smooth and includes as a particular case purely thermal convection $R_C = 0$ at $\alpha = 0$ so this regime can be identified as thermally-dominated overturning convection. At values of the other governing parameters given by (8) the flow takes the familiar form of columnar convection with $m = 9$ vertical columns arranged in a cartridge belt inside the cylinder tangent to the inner core and drifting in prograde direction ($\omega < 0$). A second abrupt transition takes place at $\alpha \approx 5\pi/16$ and brings the flow to a regime C that persist up to about $\alpha = 17\pi/32$. This range includes as a particular case purely compositional convection $R_T = 0$ at $\alpha = \pi/2$ and is, therefore, identified as compositionally-dominated overturning convection. It is interesting to note that there is a large jump in the azimuthal wave number to $m = 25$ which then monotonically decreases to $m = 8$ as the mixing angle α is increased. The convective patterns of regime C continue to drift in prograde direction. At $\alpha \approx 17\pi/32$ a last transition is observed leading to regime D that persist to $\alpha = 3\pi/4$. This regime is identified as fingering convection as it largely occupies a region where $R_T < 0$ and $R_C > 0$ corresponding to a configuration of warmer and heavier fluid over cooler and lighter fluid. The wavenumber assumes a constant value of $m = 3$ and the flow pattern drifts in prograde direction. We note that while the critical curve is single-valued when plotted in the $Ra - \alpha$ plane, it is multivalued in certain regions when plotted in the $R_C - R_T$ plane. The linear results outlined above are robust in the sense that they persist in a significant range of parameter values. For instance, [Silva et al. \(2019\)](#) report the same qualitative picture for values of the Coriolis parameter in the range $\tau \in [10^3, 10^6]$ (becoming more pronounced for larger values of τ), for values of the Prandtl number in the range $Pr \in [10^{-5}, 10^3]$ (most pronounced at intermediate values of Pr), for Schmidt to Prandtl number ratio at least within the range $Sc/Pr \in [25, 100]$, and for shell radius ratio in the range $\eta \in [0.1, 0.7]$.

4.2. Comparison with ideal estimates

It is of interest to compare these results with bounds for convective and double-diffusive instabilities known for perfect fluids. These can be summarized conveniently using the so called stability density ratio, $R_0 := (\alpha_T |\nabla T_S|) / (\alpha_C |\nabla C_S|)$, ([Stern 1960](#)). Overturning convection, semi-convection and fingering instabilities occur for values of R_0 in the intervals

$$R_0 < 1, \quad R_0 \in \left(\frac{Pr + Le^{-1}}{Pr + 1}, 1 \right), \quad R_0 \in (1, Le), \quad (9)$$

respectively, see e.g. ([Radko 2013](#), [Garaud 2018](#)), where in terms of our non-dimensional parameters the density ratio can be expressed as $R_0 = Le |R_T/R_C|$ at $r = 1$. The bound for the onset of overturning convection ($R_0 < 1$) derives from the [Ledoux \(1947\)](#) criterion for unstable stratification, $N^2 = N_T^2 + N_C^2 < 0$ where $N_T^2 := -\alpha_T \gamma \mathbf{r} \cdot \nabla T_S$ is the thermal contribution to the Brunt-Väisälä frequency N , and $N_C^2 := -\alpha_C \gamma \mathbf{r} \cdot \nabla C_S$, is the compositional contribution, respectively. Bounds (9) are shown in figures 1 and 2. Our results indicate that fingering instability occurs in stably-stratified fluids ($R_0 > 1$) in a region well captured by the bounds $R_0 \in (1, Le)$. In contrast, the semi-convection instability becomes dominant soon after the $|R_T| = |R_C|$ line is crossed and well inside the unstably-stratified region ($R_0 < 1$). This behaviour is due to the fact that the additional buoyancy provided by the compositional gradient counteracts to some extent the convection-inhibiting Coriolis force as shown by [Busse \(2002\)](#) and [Simitev \(2011\)](#). Bounds (9) must, of course, be regarded as approximate only. The Ledoux criterion is derived on the assumptions that the diffusivities and viscosity are neglected, and bounds (9) do not take into account rotation and spherical geometry effects, all essential in our configuration.

5. Finite amplitude thermo-compositional convection

In order to investigate dynamo action in the four distinct regimes of thermo-compositional convection it is first necessary to determine the regions in the parameter space that these occupy at finite-amplitudes. To trace all regimes systematically while keeping the volume of simulations at bay, we fix most of the parameter values as specified in equation (8) and vary the values of the thermal and compositional Rayleigh numbers along several selected “slices” through the $R_C - R_T$ plane as is best illustrated in figure 1(b).

Growth rates near the onset of convection will not be reported. This is because on one hand, the linear eigensolver method of [Silva *et al.* \(2019\)](#) is configured to compute the marginal stability curve where, by definition, the growth rate $\sigma = 0$. This is done by performing a non-trivial numerical extremisation and parameter continuation procedure as discussed in relation to figures 1 to 3 of ([Silva *et al.* 2019](#)). On the other hand, most of our nonlinear simulations use as their initial condition the nearest available equilibrated nonlinear solution in order to avoid long transient periods in this already computationally-expensive problem. However, nonlinear simulations are in excellent agreement with the values of the critical Rayleigh numbers predicted by the linear analysis as seen in both figures 1 and 2.

5.1. Regime boundaries

Earlier studies of purely thermal convection e.g. ([Sun *et al.* 1993](#), [Christensen 2002](#), [Simatev and Busse 2003b](#), [Busse and Simatev 2005](#), [Gillet *et al.* 2007](#)) show that immediately after onset convection assumes the form of shape-preserving columns parallel to the rotation axis and drifting in azimuthal direction with time-independent azimuthally averaged properties. From a frame of reference drifting with the convection columns the entire pattern appears steady. Differential rotation is generated through the action of Reynolds stress caused by the spiralling cross section of the columns. Further away from the onset bifurcations occur that break all available temporal and spatial symmetries of the problem and lead to flows with increasingly chaotic temporal and spacial structures and dependence. These transitions are captured well by tracking kinetic energy components e.g. ([Simatev and Busse 2003b](#), [Simatev *et al.* 2015](#)). Figure 2 shows time-averaged values of the kinetic energy density components of the flows along the selected “slices” of the $R_C - R_T$ plane and demonstrates that a similar approach is also useful in tracking double-diffusive regimes.

Increasing the value of R_T in panels 2(a) and (c) one observes the regimes of rotating fingering convection D, compositionally dominated overturning convection C and thermally dominated overturning convection B and the transitions between them. In figure 2(c), regime D appears as an isolated island of instability separated from regime C by a quiescent region. The amplitude of fingering convection motions attains a maximum at a value of R_T situated within the interior of the island of instability and decreases towards its ends. At a somewhat larger value of R_C depicted in figure 2(a), the domains of regimes D and C join up but the transition between them is well visible in the pronounced dip in kinetic energy components. An abrupt transition from regime C to regime B occurs at about $R_T = 2.7 \times 10^5$ in both panels (a) and (c) of figure 2. In figure 2(e), the transition between the regimes of rotating semi-convection A and thermally-dominated overturning convection B is shown. This transition is also abrupt and occurs at about $R_T = 2.8 \times 10^5$. The transition value $R_T = 2.8 \times 10^5$ appears to be situated along the continuation of the thermally-dominated overturning convection branch of the critical curve for the onset. Panels 2(b,d,f) show kinetic energy densities as functions of the compositional Rayleigh number R_C for several selected values of the thermal Rayleigh number R_T . Panel (b) shows the energy density components of cases in regime B. A transition to a branch with dominant differential rotation is observed at about $R_C = 9 \times 10^5$. This is a transition internal to regime B, namely a transition to chaotic convection. In figure 2(d),

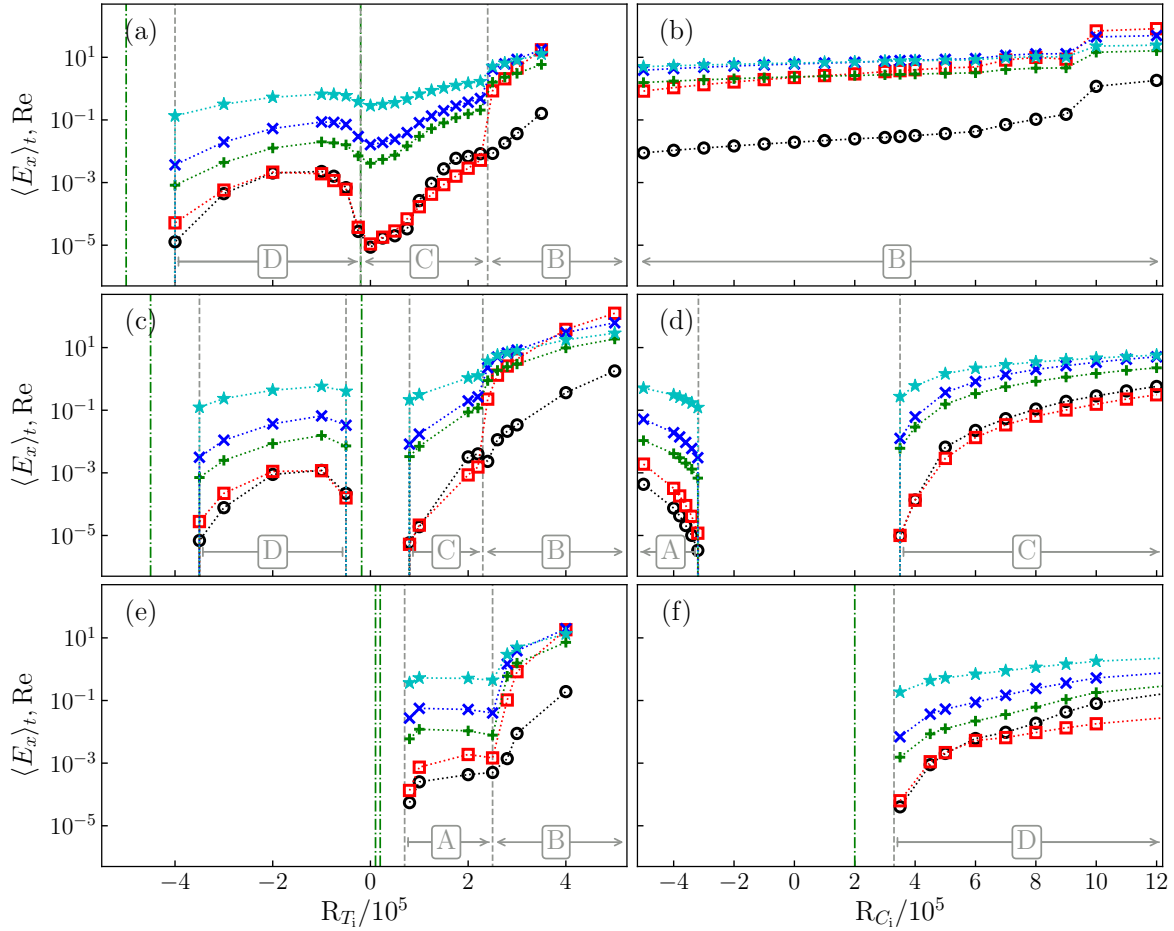


Figure 2. Time-averaged Reynolds number and kinetic energy density components in the case $\text{Pr} = 1$, $\text{Sc} = 25$, $\tau = 10^4$, $\eta = 0.35$ and (a) $R_C = 5 \times 10^5$, (b) $R_T = 3 \times 10^5$, (c) $R_C = 4.5 \times 10^5$, (d) $R_T = 2 \times 10^5$, (e) $R_C = -5 \times 10^5$, (f) $R_T = -2 \times 10^5$ as functions of R_T or R_C as appropriate. The time-averaged Reynolds numbers are denoted by cyan star symbols. The time-averaged mean poloidal component $\langle \bar{E}_p \rangle_t$, mean toroidal component $\langle \bar{E}_t \rangle_t$, fluctuating poloidal component $\langle \tilde{E}_t \rangle_t$ and fluctuating toroidal component $\langle \tilde{E}_p \rangle_t$ are indicated by a black circles, red squares, green plus signs and blue cross signs, respectively. Vertical broken lines indicate points of transition between convective regimes. The ranges over which distinct regimes are observed are indicated by arrows near the bottom abscissa. Arrowheads indicate that convection extends further and ticks at end of arrows indicate onset of convection. The locations in the $R_C - R_T$ plane of some data points used here are also denoted by red solid circles in figure 1. Where they are in the frame of the plots, stability bounds (9) are marked by vertical green dash-dotted lines from left to right as follows (a,c) $R_T = -R_C$ and $R_T = -R_C/\text{Le}$, (e) $R_T = -(\text{Pr} + 1/\text{Le})R_C/(\text{Le}(\text{Pr} + 1))$ and $R_T = -R_C/\text{Le}$, (f) $R_C = -R_T$. (Colour online)

regimes A and C are observed separated by a wide quiescent region of no convection. A gradual increase of the amplitude of the flows is seen as convection is driven away from the critical curve of linear onset. Finally, figure 2(f) shows the energy density components of flows in regime D as they are driven away from the onset neutral curve.

The fluctuating toroidal energy \tilde{E}_t and the fluctuating poloidal energy \tilde{E}_p are kinetic energy components corresponding to flows in the azimuthal direction and flows within meridional planes, respectively. These two components show very similar behaviour in all four convective regimes as seen in figure 2 because locally any flow pattern consists of both azimuthal and radial motions. The fluctuating kinetic energies dominate the flows in the regimes of rotating semiconvection A, fingering convection D, and compositionally dominated overturning convection C as well as in the vicinity of the onset transition of the regime of thermally dominated overturning convection B. It may be observed in figure 2 that in all cases the approximate relation $\langle \tilde{E}_p \rangle_t \approx 0.3 \langle \tilde{E}_t \rangle_t$ is satisfied regardless of the particular convection regime. The mean poloidal energy $\langle \bar{E}_p \rangle_t$ is the energy contained in the mean meridional circulation. Since the

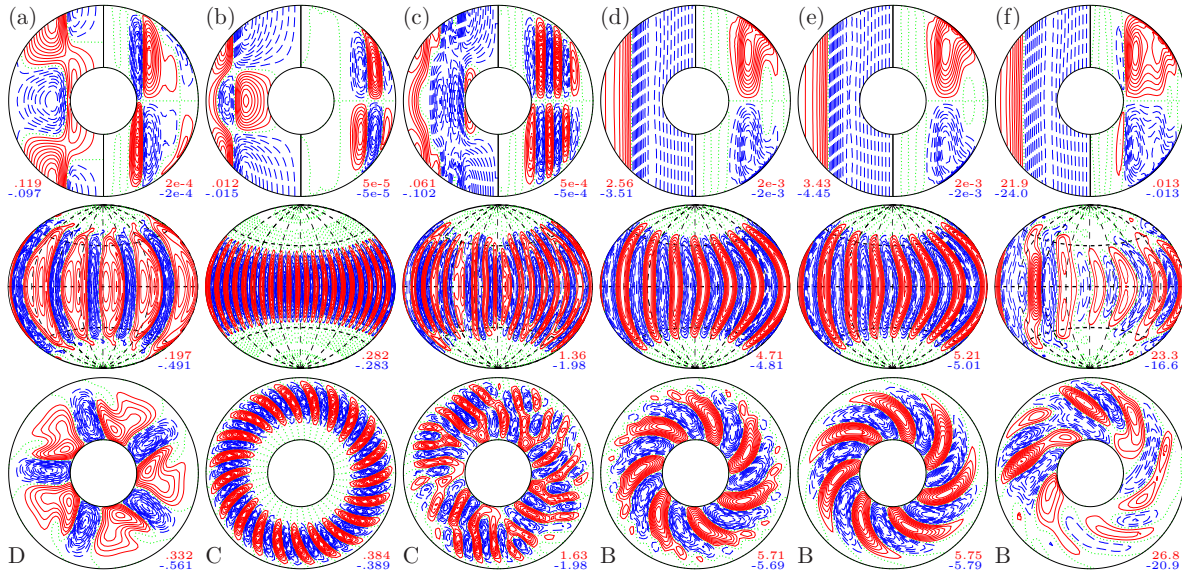


Figure 3. Flow components in the case $\eta = 0.35$, $\tau = 10^4$, $\text{Pr} = 1$, $\text{Sc} = 25$, $R_C = 4.5 \times 10^5$, and increasing values of $R_T = -2 \times 10^5, 1 \times 10^5, 2 \times 10^5, 2.8 \times 10^5, 3 \times 10^5, 5 \times 10^5$, from (a) to (f), respectively, (all part of the sequence shown in figure 2(c)). The first plot in each column shows isocontours of azimuthally-averaged \bar{u}_ϕ (left half) and streamlines $r \sin \theta (\partial_\theta \bar{v}) = \text{const.}$ (right half) in the meridional plane. The second plot shows isocontours of u_r at $r = r_i + 0.5$ mapped to the spherical surface using an isotropic Aitoff projection. The third plot shows isocontours of $r \partial_\phi v = \text{const.}$ in the equatorial plane. The minimal and the maximal values of each field are listed under the corresponding plot. The isocontours are equidistant with positive isocontours shown by solid lines, negative isocontours shown by broken lines and the zeroth isocontour shown by a dotted line in each plot. All contour plots are snapshots at a fixed representative moment in time. Labels D, C and B denote the dominant regime of convection. (Colour online)

effects of rotation strongly suppress the motions in the axial direction this component remains small, and this is seen on all convection branches in figure 2. The mean toroidal energy $\langle \bar{E}_t \rangle_t$ is the kinetic energy contained in differential rotation. On all branches shown in figure 2 except in the regime of thermally-dominated overturning convection B, the time-averaged value of $\langle \bar{E}_t \rangle_t$ is small and comparable to $\langle \bar{E}_p \rangle_t$. There are a number of reasons for this. Firstly, compositional regimes A and D appear to be limited in range and transitions to the overturning regimes B and C occur before their energy components, including $\langle \bar{E}_t \rangle_t$, can grow significantly. In addition, the two regimes A and D show broad convection structures that are not prone to spiralling, see further below. The regime of compositionally-dominated overturning convection C is characterised with a large value of the Schmidt number Sc and behaves much like purely thermal convection at large values of Pr where spiralling and consequently differential rotation is known to be weak (Simitev and Busse 2005). Differential rotation starts to grow only when the regime of thermally-dominated overturning convection B is entered. Since the toroidal fluid motions do not have a radial component, it is the poloidal motions which are directly associated with the transport of heat and material between the boundaries. The differential rotation, however, helps dynamo generation by the Ω -effect.

Regarding time-dependence, compositional regimes A and D are time-independent since transitions to regimes B and C occur before their near-onset patterns can become unstable and develop chaotic structures. Regimes B and C are time dependent and exhibit the usual sequence from steady state via time-periodic oscillations to chaotic behaviour (Simitev and Busse 2003b).

5.2. Typical flow patterns and interactions

Examples of typical flow patterns across the four convective regimes are presented in figures 3 and 4. Figure 3, in particular, includes selected cases located along the slice of the $R_C - R_T$ plane shown in figure 2(c). The first column of 3 shows a typical case in the state of rotating

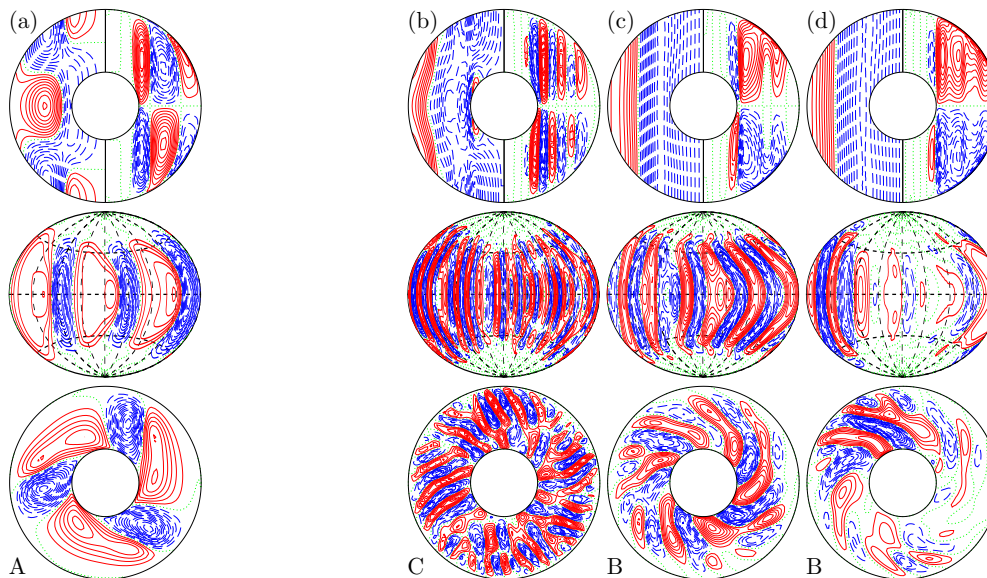


Figure 4. Flow components in the case $\eta = 0.35$, $\tau = 10^4$, $\text{Pr} = 1$, $\text{Sc} = 25$, and values of the Rayleigh numbers as follows (a) $R_C = -4 \times 10^5$ and $R_T = 2 \times 10^5$, (b) $R_C = 8 \times 10^5$ and $R_T = 2 \times 10^5$, (c) $R_C = 8 \times 10^5$ and $R_T = 4 \times 10^5$ and (d) $R_C = 8 \times 10^5$ and $R_T = 6 \times 10^5$. The same flow components are shown as in figure 3. Labels A, C and B denote the dominant regime of convection. (Colour online)

fingering convection D. At a value $R_C = -2 \times 10^5$ this case is located nearly in the middle of the regime region. The equatorial cross section of the poloidal streamlines, shown in the lowermost plot of figure 3(a), reveals a pattern of wave number 5 consisting of pairs of a narrow column with anticlockwise flow and a broad column with clockwise flow. The broad column appears as composed of two structures with clockwise flow adjacent to each other and with the one located closer to the inner core being more vigorous. The convective columns and their vertical morphology are visible in the plot of the radial velocity on a spherical surface located at the middle of the shell, shown in the middle row of figure 3(a). The plot of the radial velocity also reveals that there is little or no polar convection. Differential rotation and azimuthally averaged meridional circulation are plotted in the left and the right halves, respectively, of figure 3(a). The differential rotation profile is rather peculiar. Differential rotation is symmetric with respect to the equatorial plane and shows a prominent tube of retrograde flow situated at the equatorial region and extending to about 30° . On top of this tube there are two azimuthal jets of similarly strong prograde differential rotation. The shear layer between the jet of retrograde and the jets of prograde rotation is almost horizontal and the two prograde jets link to each other via a thin layer going behind the equatorial retrograde jet. Two weak retrograde jets are finally visible in the polar regions. The meridional circulation is antisymmetric with respect to the equatorial plane and consists of three cells oriented parallel to the axis of rotation. (Simitev and Busse 2003b, Busse and Simitev 2005).

At $R_T = 10^5$ figure 3(b) illustrates a compositionally-dominated overturning convection case in regime C as expected from linear analysis. The case is in the vicinity of the linear onset and the convection pattern changes dramatically from the case just described. The poloidal streamlines plotted in the equatorial plane exhibit a dominant azimuthal wave number of 21. The convective columns are rather thin and adjacent to the outer spherical surface rather than to the inner core. There is no polar convection as rotation inhibits polar motions. Meridional circulation is antisymmetric with respect to the equator and consists of three cells. The convection columns are spiralling very weakly and thus only weak differential rotation is generated. The differential rotation is now prograde at the outer spherical surface and at the equatorial region. Pronounced retrograde jets appear at the poles while a pronounced prograde jet appears at the inner surface near the equatorial region.

At $R_T = 2 \times 10^5$ figure 3(c) shows a more chaotic compositionally-dominated overturning convection case in regime C. The equatorial streamlines show convection columns with a wave number of 20 near the outer surface which now extend all the way to the inner core where clockwise columns coalesce to a wavenumber of about 10. The columns extend to higher latitude as seen in the plot of the radial velocity on the spherical surface. The mean meridional circulation is now five-cell and the differential rotation has become stronger with the two large polar jets extending towards the equator and coalescing.

The last three columns of figure 3 exhibit three cases of thermally-dominated convection in regime B that become increasingly chaotic with the increase of the value of R_T . The poloidal streamlines in the equatorial plane reveal a flow pattern of 7 pairs of convection columns that are anchored at the inner core and strongly spiral outwards. The mean meridional streamlines form a large one-cell antisymmetric pattern and the differential rotation exhibits a strictly geostrophic pattern constant on cylinders parallel to the tangent cylinder. The case with $R_T = 2.8 \times 10^5$ shown in figure 3(d) is situated very nearly at the transition from state C which is evidenced by a weak modulation of the convective column tips near the outer spherical surface. The case with $R_T = 5 \times 10^5$ shown in figure 3(f) is in a chaotic state known as a localized convection where differential rotation is so strong that it shears-off the convective columns so that convection is weak or suppressed in approximately half the shell volume. These properties are essentially identical to the properties of purely thermal convection at comparable parameter values

The last three columns of figure 4 also illustrate the transition from compositionally- to thermally-dominated convection, i.e. from regime C to regime B, but in a more strongly chaotic cases with a larger value of $R_C = 8 \times 10^5$. It is interesting that the C to B transition and the corresponding patterns of convection are very similar to the ones just described despite the significant increase in compositional driving.

Finally at $R_C = -4 \times 10^5$, the first column of figure 4 illustrates a typical rotating semi-convection case in regime A. An azimuthal wave-number 3 is exhibited by the poloidal streamlines in the equatorial plane. The asymmetry between narrow columns with anticlockwise flow and broad columns with clockwise flow featured in by fingering regime D is also present here. The profiles of mean meridional flow and of the differential rotation are also very similar to the corresponding patterns of the fingering regime but are in reversed direction, i.e. a similar in shape equatorial jet of differential rotation is seen however in prograde rather than in retrograde direction.

In this section cases with small to moderate driving were used in order to clearly illustrate the patterns of convection and the transitions between the four regimes of rotation double-diffusive convection. More strongly driven convection cases are presented in the next section where a sufficient intensity of the flow is a prerequisite for dynamo action.

6. Dynamos driven by thermo-compositional convection

Having determined how the four thermo-compositional regimes evolve at finite-amplitudes, in this section we describe attempts (a) to find dynamo solutions in the semi-convection and fingering regimes and (b) to assess differences between dynamos generated by thermally-dominated and chemically-dominated overturning convection.

6.1. *Dynamo action in the semi-convective and fingering regimes*

A typical dynamo generated by rotating semi-convective flows in regime A at $R_T = 2 \times 10^5$ and $R_C = -6 \times 10^6$ and a value of the magnetic Prandtl number $Pm = 300$ is presented in figure 5. This dynamo exhibits a chaotic time dependence, as shown in the lowermost plot of

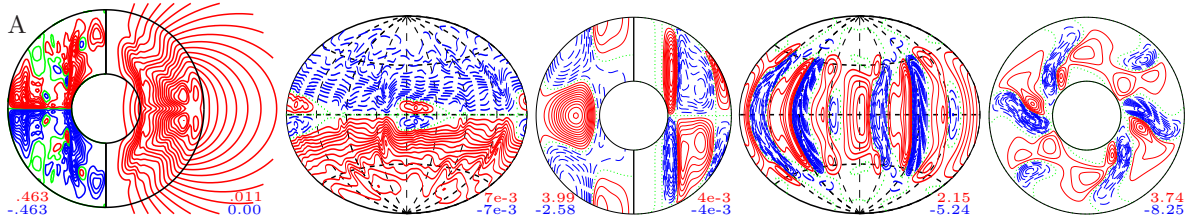


Figure 5. Flow and field structures of a dynamo in convective regime A at parameter values $\eta = 0.35$, $\tau = 10^4$, $\text{Pr} = 1$, $\text{Sc} = 25$, $R_T = 2 \times 10^5$, $R_C = -6 \times 10^6$, and $\text{Pm} = 300$. The first plot shows isocontours of $\overline{B_\phi}$ (left half) and meridional fieldlines $r \sin \theta \partial_\theta \overline{h} = \text{const.}$ (right half). The second plot shows isocontours of radial magnetic field B_r at $r = r_o + 0.1$ in isotropic Aitoff projection. The last three plots show the same flow components as in figure 3. The minimal and the maximal values of each field are listed under the corresponding plot. The isocontours are equidistant with positive isocontours shown by solid lines, negative isocontours shown by broken lines and the zeroth isocontour shown by a dotted line in each plot. All contour plots are snapshots at a fixed representative moment in time (Colour online).

figure 8(a), even though snapshots at different times remain rather similar to the one shown in figure 5. The ratio of toroidal to poloidal magnetic energy is $E_{\text{tor}}^{\text{magn}}/E_{\text{pol}}^{\text{magn}} = 9.98$ so that much of the magnetic field is confined to the core. The ratio of $E_{\text{dip}}^{\text{magn}}/E_{\text{quadr}}^{\text{magn}} = 3272.9$ so that the dynamo is almost perfectly dipolar. However, the ratio of total magnetic to total kinetic energy is rather small at $E_{\text{magn}}/E_{\text{kin}} = 0.0042$. Because the magnetic field is so weak compared to the intensity of the flow, convection is nearly unaffected by dynamo action. Indeed, the spatial patterns of the flow remain very similar to the ones described in relation to the corresponding case shown in figure 4(a). The most pronounced difference is that the dominant azimuthal wavenumber of the flow is $m = 6$, as seen in the m -spectrum of the kinetic energy in figure 8(a), and is larger than the azimuthal wave number in the non-magnetic case shown in the first column of 4(a) which is likely due to the smaller value of the compositional Rayleigh number R_C used here. A plot of the azimuthally averaged toroidal fieldlines in the meridional plane are shown in the left half of the first plot of figure 5. The plot reveals a pair of toroidal flux tubes of opposite polarity located near the outer core above and below the equator. A second pair of elongated toroidal flux parallel to the axis of rotation are situated at the cylinder tangent to the inner core. This profile of the azimuthally averaged toroidal fieldlines correlates well with the profile of the differential rotation shown in the left half of the third plot in 5 which exhibits regions of shear near the equator and on the tangent cylinder. The azimuthally averaged poloidal fieldlines in the meridional plane are shown in the right half of the first plot of figure 5 and exhibit a typical dipolar structure as also evident in by the l -spectrum of magnetic energy shown in figure 8(a). Besides the apparent large-scale dipolar field, the plot of the radial magnetic field at surface exhibits two small patches of inverted polarity near the equator. Because the ratio of total magnetic to total kinetic energy is very small while at the same time the value of the magnetic Prandtl number $\text{Pm} = 300$ needed to support dynamo action in this case is very large it is unlikely that dynamos in state A are of relevance in planetary and stellar magnetism.

We have been unsuccessful in our efforts to obtain a non-decaying dynamo in regime D of rotating fingering double-diffusive convection. The values of both Pm and R_C were increased along the line $R_T = -200000$, but with the computational constraints of the code only decaying dynamo solutions were obtained.

6.2. Dynamo action in the overturning regimes

It is of interest to investigate how the sharp transition between regimes B to C affects dynamo behaviour and whether the properties of the magnetic field also exhibit an abrupt transition. An example of a dynamo in the regime of thermally-dominated overturning convection B is presented in figure 6 at values of the magnetic Prandtl number $\text{Pm} = 15$, the compositional Rayleigh number $R_C = 1.2 \times 10^6$ and the thermal Rayleigh number $R_T = 3 \times 10^5$,

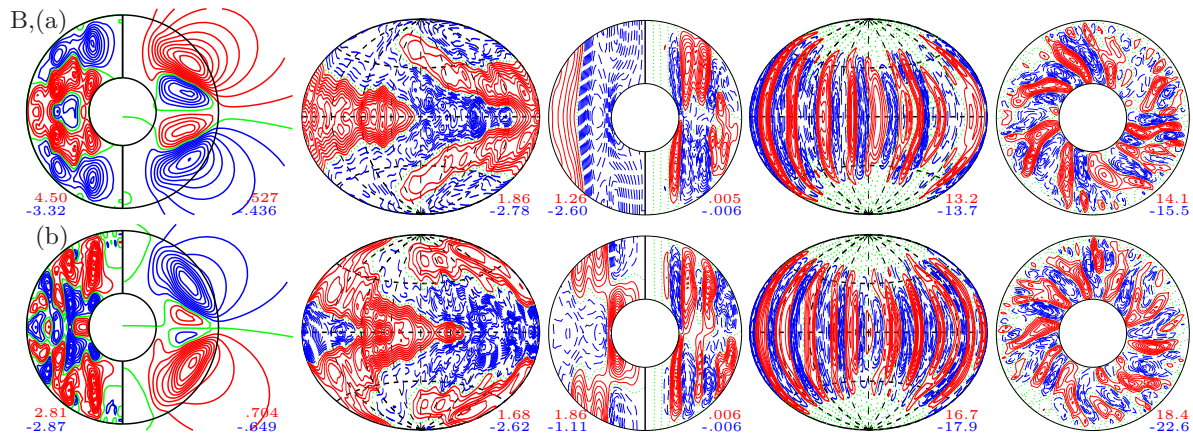


Figure 6. Oscillation of a quadrupolar dynamo in convective regime B at parameter values $\eta = 0.35$, $\tau = 10^4$, $\text{Pr} = 1$, $\text{Sc} = 25$, $R_T = 3 \times 10^5$, $R_C = 1.2 \times 10^6$, and $\text{Pm} = 15$. Snapshots are shown (a) at the beginning and (b) at the end of a half a period the oscillation with time lapse $\Delta t = 5.0$. The same flow and field components are shown as in figure 5. (Colour online)

respectively. This is a strong field dynamo with a ratio of total magnetic to kinetic energy $E_{\text{magn}}/E_{\text{kin}} = 1.01$. The predominant dynamo morphology is quadrupolar as evidenced by the the l -spectrum of magnetic energy shown in figure 8(b) and by the ratio of dipolar to quadrupolar energy components $E_{\text{dip}}^{\text{magn}}/E_{\text{quadr}}^{\text{magn}} = 0.02$. The component detectable outside of the dynamo generating region is strong as measured by the ratio of toroidal to poloidal magnetic energy $E_{\text{tor}}^{\text{magn}}/E_{\text{pol}}^{\text{magn}} = 1.22$. As is typical for quadrupolar dynamos this example exhibits regular periodic oscillations in time. The oscillations are well visible in the plots of all magnetic field components and represent a dynamo wave propagating from the equator to the poles. Emergence of magnetic flux is initiated at the equator near the inner core boundary as can be best seen in the plots of the azimuthally averaged toroidal and poloidal fieldlines in the first column of figure 6. These new flux tubes proceed to grow and drift to higher latitudes pushing old flux tubes upwards in the northern hemisphere and downwards in the southern hemisphere. At high latitudes the magnetic flux tubes in question become weaker gradually dissipate and are replaced in a similar fashion by new fluxes of the opposite polarity. The dynamo wave exhibits a phase shift in azimuthal direction in the sense that at any given moment the pole-ward drifting flux tubes appear at various latitude for various azimuthal angles thus forming a pair of V-shaped spiraling structures as seen in the contour plot of the radial magnetic field B_r . The frequency of oscillations is proportional to the square roots of the magnetic Prandtl number and the kinetic helicity and to the fourth root of the differential rotation (Busse and Simatev 2006). Although this is a strong field dynamo, flow structures are weakly affected by the magnetic field. The dominant azimuthal wavenumber of the flow is $m = 8$ as seen in the m -spectrum of the kinetic energy in figure 8(b) and other flow features remain much as described in relation to figures 3 and 4 above. An exception to this is the strong effect of the magnetic field on differential rotation which is significantly reduced in amplitude and oscillates between a geostrophic and conical profile as seen in the left half of the third column of figure 6. The weaker differential rotation is as a result less able to shear-off the azimuthally drifting convective columns. This example is very similar to oscillating quadrupolar dynamos familiar from purely-thermal models e.g. (Busse and Simatev 2005). It is perhaps surprising that a quadrupolar dynamo occurs at a rather larger value of the magnetic Prandtl number than in the former case, e.g. see figure 3 of (Busse and Simatev 2005).

Two typical dynamos in regime C of rotating compositionally-dominated overturning convection are illustrated in figure 7 at a value of the magnetic Prandtl number $\text{Pm} = 30$, a value of the compositional Rayleigh number $R_C = 1.2 \times 10^6$ and thermal Rayleigh num-

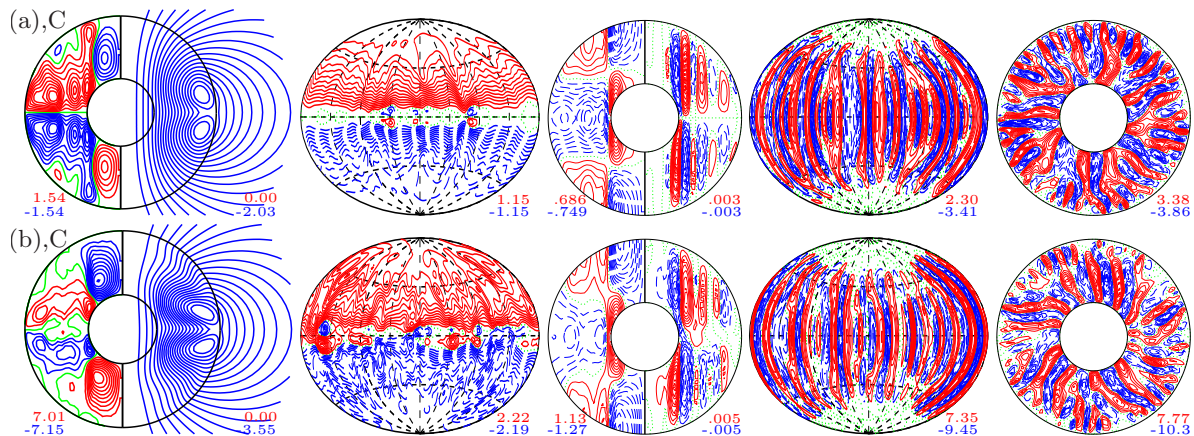


Figure 7. Two typical dynamos in convective regime C at parameter values $\eta = 0.35$, $\tau = 10^4$, $Pr = 1$, $Sc = 25$, and (a) $R_T = -2 \times 10^5$, $R_C = 1.2 \times 10^6$ and $Pm = 30$ and (b) $R_T = 2 \times 10^5$, $R_C = 1.2 \times 10^5$ and $Pm = 30$. The same flow and field components are shown as in figure 5. (Colour online)

bers $R_T = -2 \times 10^5$ and $R_T = 2 \times 10^5$, respectively. Both dynamos appear very similar, indeed. They are strong field dynamos with a ratio of total magnetic to total kinetic energy $E_{\text{magn}}/E_{\text{kin}} = 3.31$ and 2.61 the dynamos with $R_T = -2 \times 10^5$ and $R_T = 2 \times 10^5$, respectively. The predominant dynamo morphology is dipolar as evidenced also by the ratio of dipolar to quadrupolar energy components which is $E_{\text{dip}}^{\text{magn}}/E_{\text{quad}}^{\text{magn}} = 28.2$, and 8.87 for the first and the second dynamos, respectively. The dipolar structure of the second dynamo is confirmed by the l -spectrum of the magnetic energy in figure 8(c). The externally observable components the dynamos are weak as measured by the ratio of toroidal to poloidal magnetic energy and are $E_{\text{tor}}^{\text{magn}}/E_{\text{pol}}^{\text{magn}} = 0.32$ and 0.56 , for the first and the second dynamos, respectively. As is typical for dynamos dominated by dipolar components both dynamos are non-oscillatory and, while the time series of their kinetic and magnetic energy components are chaotic, the spacial patterns of the velocity and magnetic fields remain very similar to the ones shown in figure 7. The azimuthally averaged toroidal fieldlines shown in the left halves of the first column of figure 7 exhibit magnetic flux tubes antisymmetric with respect to the equator. In particular, a pair of strong flux tubes appear in the polar regions adjacent to the axes of rotation. The case with $R_T = -2 \times 10^5$ shows an equally strong pair of “butterfly” shaped flux tubes at mid to low latitudes. A similar pair appears in the case $R_T = 2 \times 10^5$ but seems to be smaller and weaker in comparison to the polar flux tubes of this case. The plots of the radial magnetic field also exhibit similar equatorially antisymmetric patterns when projected onto the spherical surface of the shell. Although both cases are strong field dynamos, their flow structures are not really affected by the magnetic field and remain much as described in relation to figures 3 and 4 above. Again an exception to this is the profound effect of the magnetic field on differential rotation which being weaker than the one of the cases in regime B, is further reduced in amplitude and is modified to assume a profile featuring a retrograde jet in the equatorial region.

It is interesting to note that an abrupt transition in magnetic field properties seem to exist when the boundary of the convective regimes B and C is traversed. Indeed, the relatively small change in the value of the thermal Rayleigh number R_T from 3×10^5 to 2×10^5 needed to transition between the dynamos shown in figures 6 and 7(b) produces magnetic fields of very different intensity and morphology. In addition, there is a pronounced difference in the value of the magnetic Prandtl number required to obtain non-decaying dynamos in the two regimes in question. Indeed, $Pm = 15$ for the example shown in figure 6 while $Pm = 30$ for the example shown in figure 7(b), with both solutions being near the onset of dynamo action.

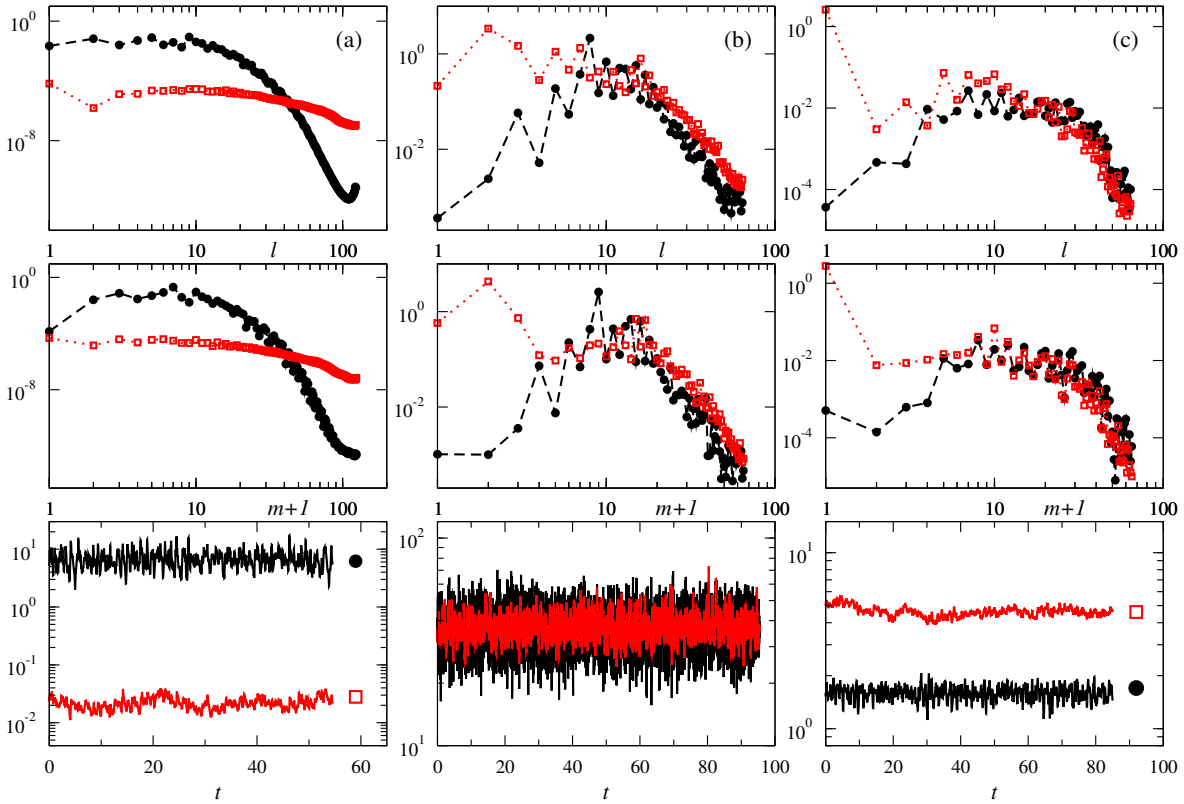


Figure 8. Instantaneous radial averages of kinetic energy spectra (black solid circles) and magnetic energy spectra (red empty squares) as functions of the spherical degree l (top row) and azimuthal order $m+1$ (middle row). The bottom row shows total kinetic energy densities (black line marked with black solid circle) and magnetic energy densities (red line marked with red empty square) as functions of time for the dynamos shown in (a) figure 5, (b) figure 6 and (c) figure 7(a). (Color online).

7. Conclusion

The main goals of this work are to establish the possibility of dynamo action arising due to double-diffusive flows on stably stratified background and to assess how dynamos generated by thermally- and chemically-dominated overturning convection differ from each other. Guided by previous linear stability analysis of the onset of convection in this configuration (Silva *et al.* 2019), we traced out in the nonlinear domain the four distinct regimes of rotating double-diffusive convection, namely rotating semi-convection, rotating thermally-dominated overturning convection, rotating compositionally-dominated overturning convection and rotating fingering convection.

Since the configuration space of the problem is now significantly larger than that of purely thermal convection, we restrict the attention to a set of carefully selected parameter values and model assumptions that allow for (a) a systematic access to all four flow regimes and at the same time (b) for direct comparison of results to purely thermal simulations readily available in the literature e.g. (Simatev and Busse 2003a, Busse and Simatev 2005; 2006). To this end, internally distributed heat and concentration sources, stress-free velocity and fixed temperature and concentration boundary conditions were used at the electrically insulating inner and outer spherical surface following the articles cited above. Both thermal and compositional Rayleigh numbers R_T and R_C were varied while all other parameters were fixed at relatively modest but computationally feasible values $Pr = 1$, $Sc = 25$, $\tau = 10^4$, $\eta = 0.35$, and the magnetic Prandtl number was selected so as to be just over the onset of dynamo action.

We find that convection instability pockets identified in the linear stability analysis (Simatev 2011, Silva *et al.* 2019) survive nonlinear interactions and that the boundaries of the four con-

vective regimes can be traced towards finite-amplitudes in the configuration space for, at least, several times the critical values of R_T and R_C . We confirm that boundaries remain sharp resulting in abrupt transitions between convective regimes as noted by [Breuer *et al.* \(2010\)](#) for the boundary between the thermally-dominated and the compositionally-dominated overturning convection at the parameter values they used. Typical velocities of flows in the semi-convecting and the fingering regimes remain relatively small compared to those in the two overturning regimes, and zonal flows remain weak in all regimes apart from the regime of thermally-dominated overturning convection. Finite-amplitude compositionally-dominated overturning convection exhibits significantly narrower azimuthal structures compared to all other regimes while the convective columns of the semi-convecting and the fingering regimes are particularly wide but with some notable asymmetry between clockwise and counter-clockwise vortices with the latter being narrower. The thermally-dominated overturning regime retain properties very similar to that of purely thermal convection, with differential rotation becoming the dominant flow component as driving is increased.

We find that dynamo action occurs in all regimes apart from the regime of fingering convection. In the latter increasing the value of the magnetic Prandtl number and venturing, as far as feasible, further out to more strongly driven flows failed to sustain the initial magnetic field seeds. Dynamo action persists in the semi-convective regime but it is very much impaired by the small intensity of the flow and the by very weak differential rotation which makes conversion of poloidal to toroidal field problematic. Unrealistically, large values of the magnetic Prandtl number were required to obtain a non-decaying dynamo solution in this case. The results of [Silva *et al.* \(2019\)](#), suggest that the region of semiconvection becomes wider as rotation is increased, and since stronger rotation also promotes stronger mean zonal flows we speculate that dynamos driven by semiconvection may be found more easily and at larger magnetic diffusivity at higher values of the Coriolis parameter τ . Both regimes of overturning convection easily support magnetic field generation. The dynamos in the thermally-dominated regime include oscillating dipolar, quadrupolar and multipolar cases similar to the ones known from our earlier parameter studies at comparable parameter values e.g. ([Simitev and Busse 2003a](#), [Busse and Simitev 2005](#); [2006](#); [2011](#)). For this reason, comparison with scaling laws for dynamos driven by thermal convection e.g. ([Christensen and Aubert 2006](#)) is not expected to yield additional insight. Due to the significantly weaker zonal flow dynamos in the compositionally-dominated regime show much more subdued temporal variation and remain predominantly dipolar as also reported by [Takahashi \(2014\)](#).

To meet the goals of this study, it was necessary to use parameter values removed from both geo- and planetary estimates. To rectify this, it is desirable to approach more ambitious values allowed by modern computing resources. In the configuration studied, we did not find a regime where stable quiescent layers or layers with a distinct flow properties form spontaneously below the core-mantle boundary and coexists with flow in the bulk. It is of significant interest ([Jones 2015](#), [Olson *et al.* 2018](#), [Wicht and Sanchez 2019](#), [Bouffard *et al.* 2019](#)) to investigate whether such layers may form under different boundary conditions for the concentration and the temperature field and or different internal source-sink distributions. These issues remain interesting avenues for future work.

Acknowledgements

This work was supported by the Leverhulme Trust [grant number RPG-2012-600].

References

- Aubert, J., Flow throughout the Earth's core inverted from geomagnetic observations and numerical dynamo models. *Geophys. J. Int.*, 2012, **192**, 537–556.
- Bouffard, M., Choblet, G., Labrosse, S. and Wicht, J., Chemical convection and stratification in the Earth's outer core. *Front. Earth Sci.*, 2019, **7**, Art. 99.
- Braginsky, S. and Roberts, P., Equations governing convection in Earth's core and the geodynamo. *Geophys. Astrophys. Fluid Dyn.*, 1995, **79**, 1–97.
- Breuer, D., Hauck, S.A., Buske, M., Pauer, M. and Spohn, T., Interior evolution of Mercury. *Space Sci. Rev.*, 2007, **132**, 229–260.
- Breuer, M., Manglik, A., Wicht, J., Trümper, T., Harder, H. and Hansen, U., Thermochemically driven convection in a rotating spherical shell. *Geophys. J. Int.*, 2010, **183**, 150–162.
- Brown, J.M., Garaud, P. and Stellmach, S., Chemical transport and spontaneous layer formation in fingering convection in astrophysics. *Astrophys. J.*, 2013, **768**, 34.
- Busse, F., Grote, E. and Simatev, R., Convection in rotating spherical shells and its dynamo action. In *Earth's Core and Lower Mantle*, edited by C. Jones and A. Soward and K. Zhang, pp. 130–152, 2003 (Taylor & Francis: London & New York).
- Busse, F. and Simatev, R., Dynamos driven by convection in rotating spherical shells. *Astr. Nachr.*, 2005, **326**, 231.
- Busse, F. and Simatev, R., Remarks on some typical assumptions in dynamo theory. *Geophys. Astrophys. Fluid Dyn.*, 2011, **105**, 234.
- Busse, F.H., Is low Rayleigh number convection possible in the Earth's core?. *Geophys. Res. Lett.*, 2002, **29**, 9.1–9.3.
- Busse, F.H. and Simatev, R., Parameter dependences of convection-driven dynamos in rotating spherical fluid shells. *Geophys. Astrophys. Fluid Dyn.*, 2006, **100**, 341–361.
- Christensen, U., Olson, P. and Glatzmaier, G.A., Numerical modelling of the geodynamo: a systematic parameter study. *Geophys. J. Int.*, 1999, **138**, 393–409.
- Christensen, U.R., Zonal flow driven by strongly supercritical convection in rotating spherical shells. *J. Fluid Mech.*, 2002, **470**, 115–133.
- Christensen, U.R. and Aubert, J., Scaling properties of convection-driven dynamos in rotating spherical shells and application to planetary magnetic fields. *Geophys. J. Int.*, 2006, **166**, 97–114.
- Garaud, P., Double-diffusive convection at low Prandtl number. *Annu. Rev. Fluid Mech.*, 2018, **50**, 275–298.
- Gillet, N., Brito, D., Jault, D. and Nataf, H.C., Experimental and numerical studies of convection in a rapidly rotating spherical shell. *J. Fluid Mech.*, 2007, **580**, 83–121.
- Glatzmaier, G.A. and Roberts, P.H., An anelastic evolutionary geodynamo simulation driven by compositional and thermal convection. *Phys. D*, 1996, **97**, 81–94.
- Hori, K., Wicht, J. and Christensen, U.R., The influence of thermo-compositional boundary conditions on convection and dynamos in a rotating spherical shell. *Phys. Earth Planet. Int.*, 2012, **196–197**, 32–48.
- Jacobson, S.A., Rubie, D.C., Hernlund, J., Morbidelli, A. and Nakajima, M., Formation, stratification, and mixing of the cores of Earth and Venus. *Earth Planet. Sci. Lett.*, 2017, **474**, 375–386.
- Jones, C.A., 8.05 - Thermal and Compositional Convection in the Outer Core. In *Treatise on Geophysics (Second Edition)*, edited by G. Schubert, pp. 115 – 159, 2015 (Elsevier: Oxford).
- Jones, C.A., Planetary magnetic fields and fluid dynamos. *Annu. Rev. Fluid Mech.*, 2011, **43**, 583–614.
- Kono, M., Recent geodynamo simulations and observations of the geomagnetic field. *Rev. Geophys.*, 2002, **40**.
- Kuang, W. and Bloxham, J., An Earth-like numerical dynamo model. *Nature*, 1997, **389**, 371–374.
- Leconte, J. and Chabrier, G., A new vision of giant planet interiors: Impact of double diffusive convection. *Astron. Astrophys.*, 2012, **540**, A20.
- Ledoux, P., Stellar models with convection and with discontinuity of the mean molecular weight. *Astrophys. J.*, 1947, **105**, 305.
- Livermore, P.W., Bailey, L.M. and Hollerbach, R., A comparison of no-slip, stress-free and inviscid models of rapidly rotating fluid in a spherical shell. *Sci. Rep.*, 2016, **6**.
- Manglik, A., Wicht, J. and Christensen, U.R., A dynamo model with double diffusive convection for Mercury's core. *Earth Planet. Sci. Lett.*, 2010, **289**, 619–628.
- Marti, P. *et al.*, Full sphere hydrodynamic and dynamo benchmarks. *Geophys. J. Int.*, 2014, **197**, 119–134.
- Matsui, H. *et al.*, Performance benchmarks for a next generation numerical dynamo model. *Geochem. Geophys. Geosys.*, 2016, **17**, 1586–1607.
- Mirouh, G.M., Garaud, P., Stellmach, S., Traxler, A.L. and Wood, T.S., A new model for mixing by double-diffusive convection (semi-convection). I. The conditions for layer formation. *Astrophys. J.*, 2012, **750**, 61.
- Moll, R., Garaud, P., Mankovich, C. and Fortney, J.J., Double-diffusive erosion of the core of Jupiter. *Astrophys. J.*, 2017, **849**, 24.
- Moll, R., Garaud, P. and Stellmach, S., A new model for mixing by double-diffusive convection (semi-convection). III. Thermal and compositional transport through non-layered ODDC. *Astrophys. J.*, 2016, **823**, 33.
- Monville, R., Vidal, J., Cébron, D. and Schaeffer, N., Rotating double-diffusive convection in stably stratified planetary cores. *Geophys. J. Int.*, 2019, **219**, S195–S218.
- Net, M., Garcia, F. and Sánchez, J., Numerical study of the onset of thermosolutal convection in rotating

- spherical shells. *Phys. Fluids*, 2012, **24**, 064101.
- Olson, P., Landeau, M. and Reynolds, E., Outer core stratification from the high latitude structure of the geomagnetic field. *Front. Earth Sci.*, 2018, **6**, Art. 140.
- Radko, T., *Double-Diffusive Convection*, 2013 (Cambridge University Press).
- Roberts, P.H. and King, E.M., On the genesis of the Earth's magnetism. *Reports on Progress in Physics*, 2013, **76**, 096801.
- Silva, L., Mather, J.F. and Simatev, R.D., The onset of thermo-compositional convection in rotating spherical shells. *Geophys. Astrophys. Fluid Dyn.*, 2019, **113**, 377–404.
- Silva, L.A.C. and Simatev, R.D., Spectral code for linear analysis of the onset of thermo-compositional convection in rotating spherical fluid shells. 2018, Technical report, Zenodo 10.5281/zenodo.1307245.
- Simatev, R. and Busse, F., Prandtl-number dependence of convection-driven dynamos in rotating spherical fluid shells. *J. Fluid Mech.*, 2005, **532**, 365–388.
- Simatev, R. and Busse, F.H., Parameter dependences of convection driven spherical dynamos. In *High Performance Computing in Science and Engineering '02*, edited by E. Krause E. and W. Jaeger, pp. 15–35, 2003a (Springer: Berlin).
- Simatev, R. and Busse, F.H., Patterns of convection in rotating spherical shells. *New J. Phys.*, 2003b, **5**, 97.1–97.20.
- Simatev, R., Double-diffusive convection in a rotating cylindrical annulus with conical caps. *Phys. Earth Planet. Int.*, 2011, **186**, 183–190.
- Simatev, R., Kosovichev, A. and Busse, F., Dynamo effects near the transition from solar to anti-solar differential rotation. *Astrophys. J.*, 2015, **810**, 80.
- Stern, M.E., The "salt-fountain" and thermohaline convection. *Tellus*, 1960, **12**, 172–175.
- Sun, Z., Schubert, G. and Glatzmaier, G., Transitions to chaotic thermal convection in a rapidly rotating spherical fluid shell. *Geophys. Astrophys. Fluid Dyn.*, 1993, **69**, 95–131.
- Takahashi, F., Double diffusive convection in the Earth's core and the morphology of the geomagnetic field. *Phys. Earth Planet. Int.*, 2014, **226**, 83–87.
- Tilgner, A., Spectral methods for the simulation of incompressible flows in spherical shells. *Int. J. Numer. Meth. Fluids*, 1999, **30**, 713–724.
- Traxler, A., Garaud, P. and Stellmach, S., Numerically determined transport laws for fingering ("thermohaline") convection in astrophysics. *Astrophys. J.*, 2011, **728**, L29.
- Trümper, T., Breuer, M. and Hansen, U., Numerical study on double-diffusive convection in the Earth's core. *Phys. Earth Planet. Int.*, 2012, **194-195**, 55–63.
- Veronis, G., Effect of a stabilizing gradient of solute on thermal convection. *J. Fluid Mech.*, 1968, **34**, 315–336.
- Wicht, J. and Tilgner, A., Theory and modeling of planetary dynamos. *Space Sci. Rev.*, 2010, **152**, 501–542.
- Wicht, J. and Sanchez, S., Advances in geodynamo modelling. *Geophys. Astrophys. Fluid Dyn.*, 2019, **113**, 2–50.
- Wong, J., Davies, C.J. and Jones, C.A., A Boussinesq slurry model of the F-layer at the base of Earth's outer core. *Geophys. J. Int.*, 2018, **214**, 2236–2249.
- Wood, T.S., Garaud, P. and Stellmach, S., A new model for mixing by double-diffusive convection (semi-convection). II. The transport of heat and composition through layers. *Astrophys. J.*, 2013, **768**, 157.